

## Article

# Current- and Voltage-Actuated Transmission Line Protection Scheme Using a Hybrid Combination of Signal Processing Techniques

Ligang Tang <sup>1,\*</sup>, Om Prakash Mahela <sup>2,3</sup>, Baseem Khan <sup>3,4</sup> and Yini Miro <sup>5,6,7</sup>

<sup>1</sup> School of Electrical and Electronic Information Engineering, Hubei Polytechnic University, Huangshi 435003, China

<sup>2</sup> Power System Planning Division, Rajasthan Rajya Vidyut Prasaran Nigam Ltd., Jaipur 302005, India

<sup>3</sup> Engineering Research and Innovation Group (ERIG), Universidad Internacional Iberoamericana, Campeche 24560, Mexico; baseem.khan1987@gmail.com

<sup>4</sup> Department of Electrical and Computer Engineering, Hawassa University, Hawassa P.O. Box 05, Ethiopia

<sup>5</sup> Higher Polytechnic School, Universidad Europea del Atlántico, C/Isabel Torres 21, 39011 Santander, Spain

<sup>6</sup> Department of Project Management, Universidad Internacional Iberoamericana, Campeche 24560, Mexico

<sup>7</sup> Department of Project Management, Universidad Internacional Iberoamericana, Arecibo 00613, Puerto Rico

\* Correspondence: tangligang@hbpu.edu.cn

† These authors contributed equally to this work.

**Abstract:** This paper presents a current- and voltage-driven protection scheme for transmission lines based on a hybrid mix of Stockwell transform (ST) and Hilbert transform (HT). Use of both current and voltage waveforms to detect and categorize faults, improves the reliability of this protection scheme and avoids false tripping. Current and voltage waveforms captured during a period of fault are analyzed using ST to compute a median intermediate fault index (MIFI), a maximum value intermediate fault index (MVFI), and a summation intermediate fault index (SIFI). Current and voltage signals are analyzed via applying HT to compute a Hilbert fault index (HFI). The proposed hybrid current and voltage fault index (HCVFI) is obtained from the MIFI, MVFI, SIFI, and HFI. A threshold magnitude for this hybrid current and voltage fault index (HCVFITH) is set to 500 to identify the faulty phase. The HCVFIT is selected after testing the method for various conditions of different fault locations, different fault impedances, different fault occurrence angles, and reverse flows of power. Fault classification is performed using the number of faulty phases and an index for ground detection (IGD). The ground involved in a fault is detected by comparison of peak IGD magnitude with a threshold for ground detection (THGD). THGD is considered equal to 1000 in this study. The study is carried out using a two-terminal transmission line modeled in MATLAB software. The performance of the proposed technique is better compared to a discrete wavelet transform (DWT)-based technique, a time–frequency approach, and an alienation method. Our algorithm effectively detected an AG fault, observed on a practical transmission line.

**Keywords:** fault event; Hilbert transform; signal processing technique; Stockwell transform; transmission line; protection scheme



**Citation:** Tang, L.; Mahela, O.P.; Khan, B.; Miro, Y. Current- and Voltage-Actuated Transmission Line Protection Scheme Using a Hybrid Combination of Signal Processing Techniques. *Sustainability* **2023**, *15*, 5715. <https://doi.org/10.3390/su15075715>

Academic Editor: George Kyriakarakos

Received: 26 December 2022

Revised: 4 March 2023

Accepted: 22 March 2023

Published: 24 March 2023



**Copyright:** © 2023 by the authors. Licensee MDPI, Basel, Switzerland. This article is an open access article distributed under the terms and conditions of the Creative Commons Attribution (CC BY) license (<https://creativecommons.org/licenses/by/4.0/>).

## 1. Introduction

Power transmission networks are continuously being expanded and becoming complex in nature, which leads to challenges such as protection of transmission lines, power system stability, voltage stability, and power quality. These grid parameters are further worsened by the integration of a high amount of renewable energy (RE), the deployment of power-converter-equipped devices, and non-linear nature loads [1]. The conventional method of fault detection on transmission lines is the use of distance relays. Generally, mal-operation of these relays is observed with power swings, load encroachment, and high impedance faults (HIFs) [2]. Currently, researchers, academics, scientists, and power

engineers are continuously working on improving transmission line fault identification techniques by application of signal processing and intelligent techniques to mitigate the limitations of conventional relays. In [3], the authors designed a self-attention convolutional neural network (SAT-CNN) technique to detect and categorize faults incident on power lines. This protection scheme used a time-series imaging-actuated feature extraction technique. Discrete wavelet transform (DWT) was implemented for de-noising voltage and current waveforms recorded during fault periods. In [4], the authors designed techniques which use data recorded using traveling waves on single-terminal parallel circuits of power lines equipped with STATCOMs to detect, locate, and identify faulty sections of lines and also faulty phases. The efficiency of the method was not degraded in the presence nor absence of the STATCOMs. In [5], the authors designed a protection algorithm using DWT and wavelet entropy to detect, classify, and locate faulty events on a transmission line equipped with flexible AC transmission system (FACTS) devices at the center of line. Analysis of both current and voltage waveforms was used to achieve the fault recognition. In [6], the authors designed three deep learning (DL) classification and regression approaches using deep recurrent neural networks (DRNN) for fault region identification (FRI), fault type classification (FTC), and fault location prediction (FLP) for a power line. These models used the transient data of before-fault and after-fault cycles of current and voltage waveforms at both terminals of the power line. These models achieved better detection, classification, and location accuracy relative to contemporary techniques. A quality optimization technique for a transmission line fault detection method using an embedded chip was designed in [7]. It is based on the application of reflection and transmission coefficients of the transmission line, attenuation laws of voltage waves, and current waves. It was established that the optimization technique combined with an embedded chip improved the efficiency of fault detection. In [8], authors introduced a fault detection approach using alienation coefficients of current waveforms for parallel circuits of transmission lines. This effectively detected the faults in a quarter cycle period. In [9], the authors designed a fuzzy-logic-supported algorithm for fault detection and classification of series faults incident on a six phase transmission line. This method is effective in detecting and classifying different types of series faults, incident at different locations, with various fault inception angles. In [10], the authors described a power line fault identification method using wavelet transform (WT) and linear discriminant analysis (LDA). Fault identification was achieved by processing the current waveform, and zero sequence currents were analyzed to detect ground involvement.

A detailed analysis of papers, described in the above paragraph, was performed and we hypothesized that the performance of protection schemes can be improved using a hybrid combination of signal processing approaches to process both current and voltage signals. This was taken as the research objective in this manuscript and the following are our research contributions:

- Current-actuated parameters, such as the current-based median index (CMI), the current-based maximum value index (CMVI), the current-based summation index (CSI), and the current-based co-variance index (CCI) were computed by decomposition of current waveforms using ST. The Hilbert current index (HCI) was computed by decomposition of current waveforms using HT.
- Voltage-actuated parameters such as the voltage-based median index (VMI), the voltage-based maximum value index (VMVI), the voltage-based summation index (VSI), and the voltage-based co-variance index (VCI) were computed by processing voltage waveforms using ST. The Hilbert voltage index (HVI) was computed by processing voltage waveforms using HT.
- MIFI, MVFI, SIFI, CVIFI, and HIFI were computed using the current- and voltage-actuated parameters.
- The proposed hybrid current and voltage fault index (HCVFI) was computed by multiplication of MIFI, MVFI, SIFI, CVIFI, HIFI, and a weight factor (WF). Faults were

identified by comparing the maximum value of HCVFI, which is considered equal to 500, with the hybrid current and voltage fault index (HCVFITH).

- Fault classification was achieved using an index for ground detection (IGD) and the number of faulty phases. IGD was computed by decomposing the zero sequence current using ST.
- The proposed method is effective in detecting and classifying fault events such as AG, AB, ABG, ABC, and ABCG. It effectively detected faults during various cases such as variable fault impedances, fault occurrence angles, and fault locations. It also effectively detected the fault on a practical transmission line. It is effective compared to other fault detection methods using DWT, a time–frequency approach, or an alienation coefficient.

Eight sections are used to arrange the contents of paper. The introduction is the first section. A discussion of the reported research, the existing research gap, our research contribution, and the paper structure are discussed in this section. The test transmission line is discussed in Section 2. Section 3 elaborates on the fault recognition method and related mathematical formulas. Section 4, discusses the simulation results of fault identification and classification. The simulation results of testing the technique during various case studies are elaborated on in Section 5. Section 6, details the results of testing the algorithm in detecting a fault that had occurred on a practical power line. A comparative study to analyze the effectiveness of the proposed method is included in Section 7. Our research is concluded in Section 8.

## 2. Test Transmission Line

The current study is validated using a two-terminal transmission line which is depicted in Figure 1 [11]. Utility generator-1 (UG-1) and utility generator-2 (UG-2) represent the large area utility grids between which the test transmission line is connected. In general this test transmission line may be considered an inter-state transmission line (ISTS). The circuit breakers (CB) CB-1 and CB-2 are equipped on both sides of bus-1. CB-3 and CB-4 are equipped on both sides of bus-2. Circuit breaker CB-2 is utilized to trip the transmission line when a faulty event is incident on the line. A current transformer (CT) placed near bus-1 records the current, and a potential transformer (PT) installed on bus-1 captures the voltage signal. These voltage and current signals are processed with the help of a designed protection algorithm, and a trip command is initiated to actuate tripping of the power line. In this study, bus-1 is taken as the sending end of the test line, and bus-2 is considered the receiving end of the power line. The test transmission line parameters are elaborated on in Table 1 [12].

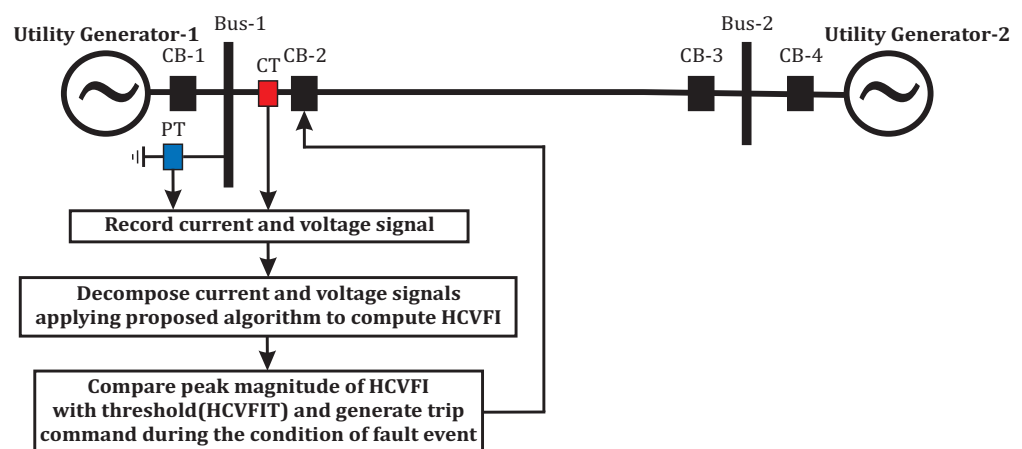


Figure 1. Test power line and installation of protection scheme [11].

**Table 1.** Magnitude of HCVFI during faulty conditions.

S. No.	Parameter	Magnitude of Parameter
1	Line length	150 km
2	UG-1 voltage	500 ∠ 20° kV
3	UG-2 voltage	500 ∠ 0° kV
4	UG-1 equivalent impedance	17.177 + j45.529 Ω
5	UG-2 equivalent impedance	15.31 + j45.925 Ω
6	Line positive sequence impedance	4.983 + j117.83 Ω
7	Line zero sequence impedance	12.682 + j364.196 Ω
8	Line positive sequence admittance	j1.468 mΩ
9	Zero sequence admittance of transmission line	j1.099 mΩ
10	Line power transfer capacity	433.63 + j294.52 MVA

### 3. Current- and Voltage-Actuated Protection Scheme

This section elaborates on the current- and voltage-actuated fault detection and classifications steps of the presented protection scheme for a power line. A detailed description of the proposed method is illustrated in Figure 2 [11].

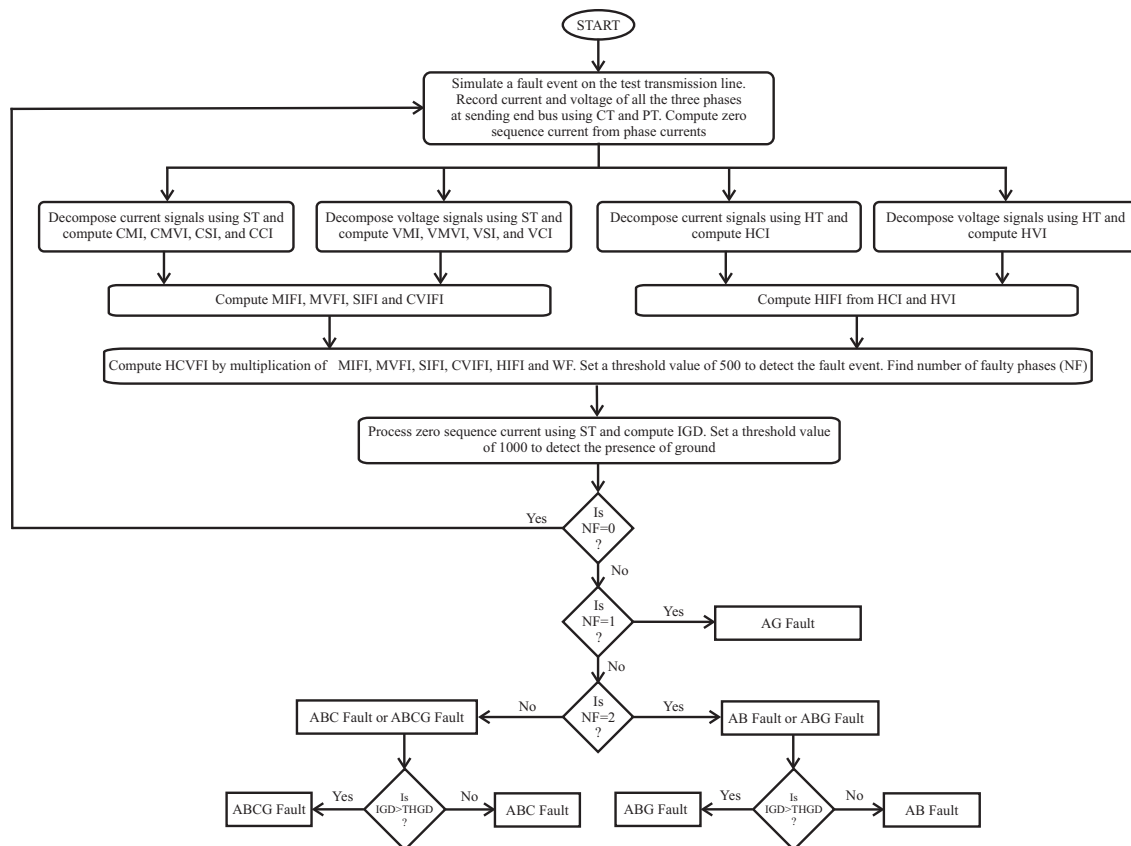


**Figure 2.** Fault estimation and categorization algorithm [11].

#### 3.1. Fault Detection

Current- and voltage-actuated fault detection can be achieved using the steps detailed below.

### 3.1.1. Current-Actuated Parameters

The current-actuated parameters are computed using the following steps:

- Realize a fault at the center of the test power line and record the currents using the CT installed near bus-1.
- Process the current signal of phase-A ( $i_1(t)$ ) using ST and take the absolute values of the output matrix to compute an ST output matrix with absolute values ( $STMAVC_1$ ) using the following expression [13,14]:

$$STMAVC_1(\tau, f) = abs \left( \int_{-\infty}^{+\infty} i_1(t) \frac{|f|}{\sqrt{2\pi}} e^{-\frac{f^2(\tau-t)^2}{2}} e^{-j2\pi ft} dt \right) \quad (1)$$

The ST is taken as an extended form of continuous wavelet transform (CWT) which is computed using short-time Fourier transform (STFT) to obtain a high time resolution at a high frequency and a low time resolution at a low frequency [14]. The performance of ST is the least affected by noise superimposed on current waveforms [15]. Similarly, process the currents of phase-B ( $i_2(t)$ ) and phase-C ( $i_3(t)$ ) to compute  $STMAVC_2$  and  $STMAVC_3$ , respectively.

- Calculate the current-based median index (CMI1) for phase-A from  $STMAVC_1$  using the formula detailed below:

$$CMI1 = median(STMAVC_1) \quad (2)$$

Similarly, the current-based median indices  $CMI2$  and  $CMI3$  for phase-B and phase-C are computed from  $STMAVC_2$  and  $STMAVC_3$ , respectively.

- Calculate the current-based maximum value index (CMVI1) for phase-A from  $STMAVC_1$  using the formula detailed below:

$$CMVI1 = max(STMAVC_1) \quad (3)$$

Similarly, the current-based maximum value indices  $CMVI2$  and  $CMVI3$  for phase-B and phase-C are computed from  $STMAVC_2$  and  $STMAVC_3$ , respectively.

- Calculate the current-based summation index (CSI1) for phase-A from  $STMAVC_1$  using the formula detailed below:

$$CSI1 = sum(STMAVC_1) \quad (4)$$

Similarly, the current-based summation indices  $CSI2$  and  $CSI3$  for phase-B and phase-C are computed from  $STMAVC_2$  and  $STMAVC_3$ , respectively.

- Calculate the current-based co-variance index (CCI1) for phase-A from  $STMAVC_1$  using the formula detailed below:

$$CCI1 = cov(max(STMAVC_1)) \quad (5)$$

Similarly, the current-based co-variance indices  $CCI2$  and  $CCI3$  for phase-B and phase-C are computed from  $STMAVC_2$  and  $STMAVC_3$ , respectively.

- Process the current signal of phase-A ( $i_1(t)$ ) using HT and take the absolute magnitudes of the output matrix to compute an HT output matrix with absolute values which is designated as Hilbert current index for phase-A (HCI1) using the following expression:

$$HCI1 = abs \left( \frac{1}{\pi} \int_{-\infty}^{+\infty} \frac{i_1(t)}{t-\tau} d\tau \right) \quad (6)$$

Similarly, process the currents of phases-B and C to compute HCI2 and HCI3 for these phases, respectively.

### 3.1.2. Voltage-Actuated Parameters

The voltage-actuated parameters are computed using the following steps:

- Realize a fault at the center of the test power line and record the voltage signals using the PT installed on bus-1.
- Process the voltage signal of phase-A ( $v_1(t)$ ) using ST and take the absolute values of the output matrix to compute an ST output matrix with absolute values (STMAVV) by use of the following expression:

$$STMAVV_1(\tau, f) = abs\left(\int_{-\infty}^{+\infty} v_1(t) \frac{|f|}{\sqrt{2\pi}} e^{-\frac{f^2(\tau-t)^2}{2}} e^{-j2\pi ft} dt\right) \quad (7)$$

Similarly, process the voltages of phase-B ( $v_2(t)$ ) and phase-C ( $v_3(t)$ ) to compute  $STMAVV_2$  and  $STMAVV_3$ , respectively.

- Calculate the voltage-based median index (VMI1) for phase-A from  $STMAVV_1$  using the formula detailed below:

$$VMI1 = median(STMAVV_1) \quad (8)$$

Similarly, the voltage-based median indices  $VMI2$  and  $VMI3$  for phase-B and phase-C are computed from  $STMAVV_2$  and  $STMAVV_3$ , respectively.

- Calculate the voltage-based maximum value index (VMV1) for phase-A from  $STMAVV_1$  using the formula detailed below:

$$VMV1 = max(STMAVV_1) \quad (9)$$

Similarly, the voltage-based maximum value indices  $VMV2$  and  $VMV3$  for phase-B and phase-C are computed from  $STMAVV_2$  and  $STMAVV_3$ , respectively.

- Calculate the voltage-based summation index (VSI1) for phase-A from  $STMAVV_1$  using the formula detailed below:

$$VSI1 = sum(STMAVV_1) \quad (10)$$

Similarly, the voltage-based summation indices  $VSI2$  and  $VSI3$  for phase-B and phase-C are computed from  $STMAVV_2$  and  $STMAVV_3$ , respectively.

- Calculate the voltage-based co-variance index (VCI1) for phase-A from  $STMAVV_1$  using the formula detailed below:

$$VCI1 = cov(max(STMAVV_1)) \quad (11)$$

Similarly, the voltage-based co-variance indices  $VCI2$  and  $VCI3$  for phase-B and phase-C are computed from  $STMAVV_2$  and  $STMAVV_3$ , respectively.

- Process the voltage signal of phase-A ( $v_1(t)$ ) using HT and take the absolute magnitudes of the output matrix to compute an HT output matrix with absolute values which is designated as Hilbert voltage index for phase-A (HVI1) using following expression:

$$HVI1 = abs\left(\frac{1}{\pi} \int_{-\infty}^{+\infty} \frac{v_1(t)}{t - \tau} d\tau\right) \quad (12)$$

Similarly, process the voltages of phase-B and C to compute HVI2 and HVI3 for phase-B and C, respectively.

### 3.1.3. Computation of MIFI

The median intermediate fault indices (MIFI) for phase-A (MIFI1), B (MIFI2), and C (MIFI3) are computed by multiplication of CMI and VMI of phase-A, B, and C as detailed below:

$$MIFI1 = CMI1 \times VMI1 \quad (13)$$

$$MIFI2 = CMI2 \times VMI2 \quad (14)$$

$$MIFI3 = CMI3 \times VMI3 \quad (15)$$

### 3.1.4. Computation of Maximum Value Fault Indices

The maximum value fault indices (MVFI) for phase-A (MVFI1), B (MVFI2), and C (MVFI3) are computed by multiplication of CMVI and VMVI of the phase-A, B, and C as detailed below:

$$MVFI1 = CMVI1 \times VMVI1 \quad (16)$$

$$MVFI2 = CMVI2 \times VMVI2 \quad (17)$$

$$MVFI3 = CMVI3 \times VMVI3 \quad (18)$$

### 3.1.5. Computation of Summation Intermediate Fault Indices

The summation intermediate fault indices (SIFI) for phase-A (SIFI1), B (SIFI2), and C (SIFI3) are computed by multiplication of CSI and VSI of the phase-A, B, and C as detailed below:

$$SIFI1 = CSI1 \times VSI1 \quad (19)$$

$$SIFI2 = CSI2 \times VSI2 \quad (20)$$

$$SIFI3 = CSI3 \times VSI3 \quad (21)$$

### 3.1.6. Computation of Co-Variance Intermediate Fault Indices

The co-variance intermediate fault indices (CVIFI) for phase-A (CVIFI1), B (CVIFI2), and C (CVIFI3) are computed by multiplication of CCI and VCI of the phase-A, B, and C as detailed below:

$$CVIFI1 = CCI1 \times VCI1 \quad (22)$$

$$CVIFI2 = CCI2 \times VCI2 \quad (23)$$

$$CVIFI3 = CCI3 \times VCI3 \quad (24)$$

### 3.1.7. Computation of Hilbert Intermediate Fault Indices

The Hilbert intermediate fault indices (HIFI) for phase-A (HIFI1), B (HIFI2), and C (HIFI3) are evaluated by multiplying the HCI and HVI of phase-A, B, and C as detailed below:

$$HIFI1 = HCI1 \times HVI1 \quad (25)$$

$$HIFI2 = HCI2 \times HVI2 \quad (26)$$

$$HIFI3 = HCI3 \times HVI3 \quad (27)$$

### 3.1.8. Computation of Hybrid Current and Voltage Fault Indices

Calculate the proposed hybrid current and voltage fault indices (HCVFI) for phase-A (HCVFI1), B (HCVFI2), and C (HCVFI3) by multiplication of MIFI, MVFI, SIFI, CVIFI, HIFI, and a weight factor (WF) as detailed below:

$$HCVFI1 = MIFI1 \times MVFI1 \times SIFI1 \times CVIFI1 \times HIFI1 \times WF \quad (28)$$

$$HCVFI2 = MIFI2 \times MVFI2 \times SIFI2 \times CVIFI2 \times HIFI2 \times WF \quad (29)$$

$$HCVFI3 = MIFI3 \times MVFI3 \times SIFI3 \times CVIFI3 \times HIFI3 \times WF \quad (30)$$

Here, the weight factor (WF) is considered equal to  $1.2 \times 10^3$ . We decided on a threshold magnitude for the hybrid current- and voltage fault index (HCVFITH) equal to 500 for estimation of faults. HCVFITH was set to 500 after testing the protection algorithm for various fault conditions such as fault location at different points of line, different fault

impedances, different fault occurrence angles on waveforms, and reverse power flows on the test line.

### 3.2. Fault Classification

Faults are grouped in three groups, using the number of faulty phases which is computed by comparing the HCVFI of every phase with the HCVFITH. The first fault group (FFG) contains faults such as AG, BG, and CG, where only one phase is faulty, for which the HCVFI is higher compared to the HCVFITH. The second fault group (SFG) contains faults such as AB and ABG, where two phases are faulty. The third fault group (TFG) contains faults such as ABC and ABCG, where all phases are faulty. Faults in the SFG and TFG are discriminated from each other using an index for ground detection (IGD). The IGD is computed by processing zero sequence currents by application of an ST-based ground detection approach as discussed below. The zero sequence current ( $I_0$ ) is obtained from the phase currents using the relation detailed below:

$$I_0 = \frac{I_1 + I_2 + I_3}{3} \quad (31)$$

Process zero sequence currents ( $I_0$ ) by application of ST and take the absolute values of the output matrix (STZCA) using the following expression:

$$STZCA = abs\left(\int_{-\infty}^{+\infty} I_0(t) \frac{|f|}{\sqrt{2\pi}} e^{-\frac{f^2(\tau-t)^2}{2}} e^{-j2\pi ft} dt\right) \quad (32)$$

Calculate the median zero sequence index (MZSI) from STZCA using the formula detailed below:

$$MZSI = median(STZCA) \quad (33)$$

Calculate the maximum value zero sequence index (MVZSI) for phase-A from STZCA using the formula detailed below:

$$MVZSI = max(STZCA) \quad (34)$$

Calculate the summation zero sequence index (SZSI) for phase-A from STZCA using the formula detailed below:

$$SZSI = sum(STZCA) \quad (35)$$

Calculate the co-variance zero sequence index (CVZSI) for phase-A from STZCA using the formula detailed below:

$$CVZSI = cov(max(STZCA)) \quad (36)$$

The index for ground detection (IGD) is computed by multiplication of MZSI, MVZSI, SZSI, and CVZSI as described below:

$$IGD = MZSI \times MVZSI \times SZSI \times CVZSI \quad (37)$$

Involvement of ground is detected by comparing the maximum magnitude of IGD with the threshold for ground detection (THGD). The THGD is set to 1000. IGD is effective in discriminating AB and ABG faults. Similarly, it is also effective in discriminating ABC and ABCG faults.

## 4. Discussion of Simulation Results

The results for the estimation and classification of faults on the test line by application of the proposed current- and voltage-actuated protection method are elaborated on in this section.

#### 4.1. Fault Detection

The investigated fault events include phase-A to ground (AG) faults, faults between phase-A and phase-B (AB), faults between phase-A, phase-B, and ground (ABG), faults between three phases (ABC), and faults between three phases and ground (ABCG). Detailed results on detection of the investigated faults are elaborated on in this section.

##### 4.1.1. AG Fault

An AG fault is realized in the middle of the test line (75 km from bus-1). The currents and voltages of all phases are captured on bus-1 of the power line. Current waveforms of all phases are depicted in Figure 3. The voltage waveforms of all phases are depicted in Figure 3b. These currents and voltages are decomposed applying ST to compute MIFI, MVFI, and SIFI, which are detailed in Figure 3c–e, in respective sequence. The current and voltage signals are also decomposed using HT and Hilbert fault indices (HFI) are obtained, which is depicted in Figure 3f. The HCVFI is evaluated using the designed method, which is depicted in Figure 3g.

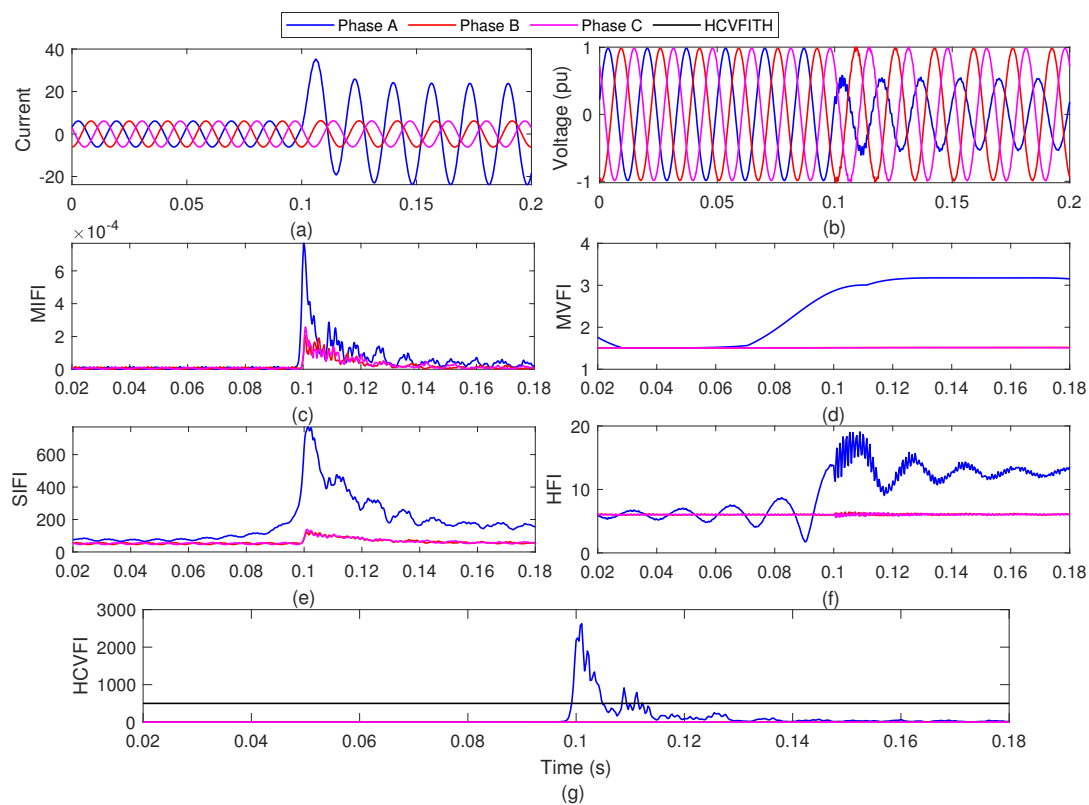


**Figure 3.** Estimation of AG faults using the current- and voltage-actuated protection method. (a) Currents of all phases, (b) voltages of all phases, (c) MIFI, (d) MVFI, (e) SIFI, (f) HFI, and (g) HCVFI.

Figure 3a depicts that the current of phase-A is increased after AG fault occurrence, whereas the currents of phase-B and C retain the values of the pre-fault scenario and the sinusoidal nature is maintained similar to that of a healthy scenario. Figure 3b depicts that the voltage of phase-A is decreased after AG fault occurrence and the voltages of phase-B and C maintained the sinusoidal nature of the healthy scenario. Figure 3c depicts that the voltage-based MIFI are increased after fault occurrence for every phase. Figure 3d details that the values of the voltage-based MVFI of the faulty phase-A change and deviate from straight line nature. The MVFI magnitudes of phase-B and C, which are healthy, are retained compared to the pre-fault scenario. Figure 3e depicts that the SIFI of all phases are increased after fault incidence. However, the increase in SIFI of the faulty phase-A is high compared to the healthy phase-B and C. Figure 3f depicts that the HFI of the

faulty phase-A is increased after fault. However, the HFI of the healthy phase-B and C are similar to those of pre-fault time. Figure 3g depicts that the HCVFI of the faulty phase-A is increased after the fault and becomes high relative to the HCVFITH, which indicates the faulty nature of phase-A. However, the HCVFI for phase-B and C is similar to and below the HCVFITH, which indicates the healthy nature of the phases. Hence, AG fault incidents are recognized effectively using the proposed current- and voltage-actuated protection scheme. The magnitudes of the HCVFI for all the phases in the event of an AG fault are included in Table 2. It is seen that the HCVFI of phase-A has high values and the HCVFI of phase-B and C are near zero.

**Table 2.** Magnitudes of HCVFI for investigated faults.

Fault Name	HCVFI		
	Phase-A	Phase-B	Phase-C
AG	$1.1596 \times 10^5$	$2.9253 \times 10^{-9}$	$6.1953 \times 10^{-10}$
AB	$3.4410 \times 10^6$	$7.6077 \times 10^5$	$1.9314 \times 10^{-11}$
ABG	$6.7301 \times 10^6$	$4.8628 \times 10^6$	$1.3624 \times 10^{-8}$
ABC	$4.9292 \times 10^6$	$3.7025 \times 10^7$	$3.1787 \times 10^7$
ABCG	$4.9292 \times 10^6$	$3.7025 \times 10^7$	$3.1787 \times 10^7$

#### 4.1.2. AB Fault

An AB fault is realized in the middle of the healthy test line (75 km from bus-1). The currents and voltages of all phases are recorded on bus-1 of the healthy line. The current waveforms of all phases are depicted in Figure 4. The voltage waveforms of all phases are depicted in Figure 4b. These currents and voltages are decomposed applying ST to compute MIFI, MVFI, and SIFI, which are detailed in Figure 4c–e, in respective sequence. The current and voltage signals are also decomposed using HT and Hilbert fault indices (HFI) are obtained, which are depicted in Figure 4f. The HCVFI is evaluated using the designed method, which is depicted in Figure 4g.

Figure 4a depicts that the currents of phase-A and B are increased after AB fault occurrence, whereas the current of phase-C follows a sinusoidal nature similar to pre-fault time. Figure 4b depicts that the voltages of phase-A and B are decreased after AB fault occurrence, whereas the voltage of phase-C follows a sinusoidal nature similar to pre-fault time. Figure 4c depicts that the MIFI is increased after AB fault, whereas the MIFI of phase-C has a low magnitude. Figure 4d depicts that the MVFI of the faulty phase-A and B are changed and deviate from a straight line nature. However, the MVFI of the healthy phase-C is similar to pre-fault time. Figure 4e depicts that the SIFI is increased after AB fault occurrence. However, the SIFI of the healthy phase-C is increased by a small amount compared to those of the faulty phase-A and B. Figure 4f depicts that the HFI of the faulty phase-A and B are increased after AB fault condition. However, the HFI of the healthy phase-C is similar to the pre-fault scenario. Figure 4g indicates that the HCVFI of the faulty phase-A and B are increased after AB fault and become higher than the HCVFITH, which indicates the faulty nature of phase-A and B. However, the HCVFI of phase-C is similar to that of pre-fault time and lower compared to the HCVFITH, indicating the healthy nature of this phase. Hence, AB faults are identified effectively using the proposed current- and voltage-actuated protection scheme.

The HCVFI of all phases during an AB fault event are detailed in Table 2. It can be seen that the HCVFI for phase-A and B are high, whereas the value of phase-C is very low.

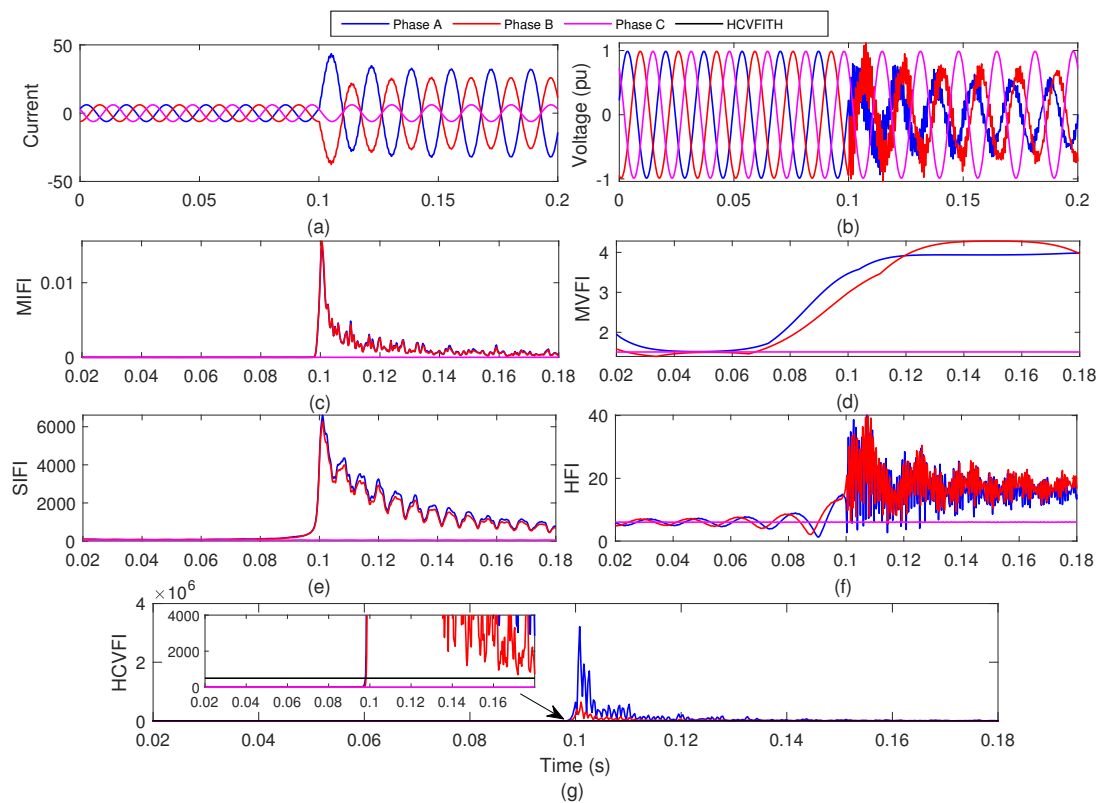


**Figure 4.** Estimation of AB faults using the current- and voltage-actuated protection method. (a) Currents of all phases, (b) voltages of all phases, (c) MIFI, (d) MVFI, (e) SIFI, (f) HFI, and (g) HCVFI.

#### 4.1.3. ABG Fault

An ABG fault is realized at the center of the test line (75 km from bus-1). The currents and voltages of all phases are captured on bus-1 of the line. Current waveforms of all phases are depicted in Figure 5a. The voltage waveforms of all phases are depicted in Figure 5b. These currents and voltages are decomposed applying ST to compute MIFI, MVFI, and SIFI, which are detailed in Figure 5c–e, in respective sequence. The current and voltage signals are also decomposed using HT and Hilbert fault indices (HFI) are obtained, which is depicted in Figure 5f. The HCVFI is evaluated using the designed method, which is depicted in Figure 5g.

Figure 5a indicates that currents of phase-A and B are increased due to ABG fault occurrence, whereas the magnitude of the current of phase-C sustains its sinusoidal waveform similar to the healthy period. Figure 5b indicates that the voltages of phase-A and B are decreased during post-fault time of ABG faults, whereas the voltage of phase-C sustains its sinusoidal waveform similar to the healthy period. Figure 5c indicates that the magnitude of the MIFI is increased for phase-A and B due to ABG faults whereas the MIFI of phase-C has low values. Figure 5d indicates that the MVFI of faulty phase-A and B change and deviate from a straight line nature. However, the MVFI of the healthy phase-C is the same in post-fault conditions and in the pre-fault period. Figure 5e indicates that the SIFI are increased due to ABG fault conditions for phase-A and B. However, the increase in the SIFI of the healthy phase-C is small in comparison to the faulty phase-A and B. Figure 5f describes that the HFI of the faulty phase-A and B are increased due to occurrence of ABG faults. However, the HFI of the healthy phase-C is similar to that observed in pre-fault time. Figure 5g indicates that the HCVFI of the faulty phase-A and B are increased due to ABG fault occurrence and become higher than the threshold HCVFITH, indicating the faulty nature of phase-A and B. However, the values of the HCVFI for phase-C in post-fault conditions are lower than HCVFITH, indicating the healthy nature of this phase. Hence, ABG

faults are effectively recognized by the use of the proposed current- and voltage-actuated protection scheme.

The values of the HCVFI of every phase during an ABG fault are provided in Table 2. It is observed that the HCVFI of phase-A and B have high magnitudes, whereas the HCVFI of phase-C has a small magnitude.

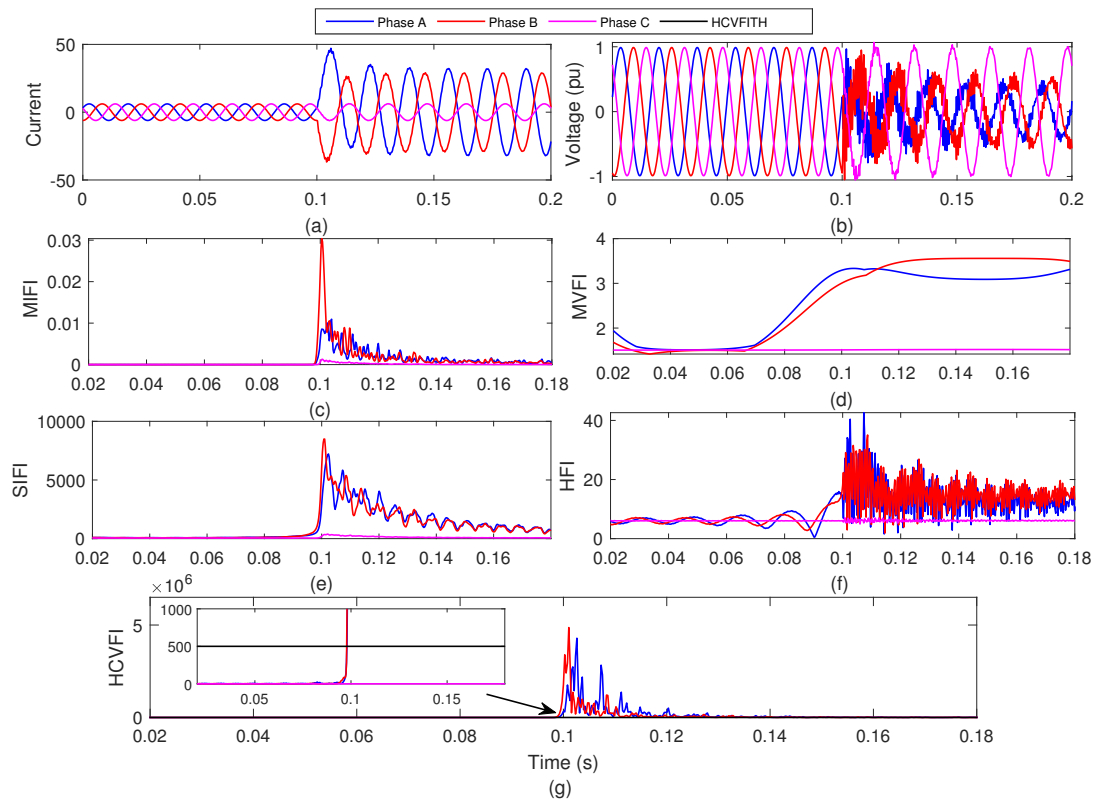


**Figure 5.** Estimation of ABG faults using the current- and voltage-actuated protection method. (a) Currents of all phases, (b) voltages of all phases, (c) MIFI, (d) MVFI, (e) SIFI, (f) HFI, and (g) HCVFI.

#### 4.1.4. ABC Fault

An ABC fault is realized at the center of the test line (75 km from bus-1). The currents and voltages of all phases are captured on bus-1 of line. Current waveforms of all phases are depicted in Figure 6a. The voltage waveforms of all phases are depicted in Figure 6b. These currents and voltages are decomposed applying ST to compute MIFI, MVFI, and SIFI, which are detailed in Figure 6c–e, in respective sequence. The current and voltage signals are also decomposed using HT and Hilbert fault indices (HFI) are obtained, which is depicted in Figure 6f. The HCVFI is evaluated using the designed method, which is depicted in Figure 6g.

Figure 6a indicates that the currents of all phases are increased due to ABC faults. Figure 6b details that the voltages associated with all phases decrease due to ABC faults. Figure 6c details that the MIFI of all phases is increased due to ABC faults. Figure 6d indicates that the MVFI of all phases change and deviate from a straight line nature. Figure 6e details that the values of current- and voltage-based SIFI are increased due to ABC faults. Figure 6f describes that the HFI of all phases are increased after ABC fault occurrence. Figure 6g details that the HCVFI of all phases is increased after ABC fault occurrence and becomes higher than the threshold HCVFITH, indicating the faulty nature of these phases. Hence, ABC faults are identified efficiently using the proposed current- and voltage-actuated protection scheme.

The values of the HCVFI of all phases for an ABC fault are included in Table 2. It is seen that the HCVFI for all phases have high values.

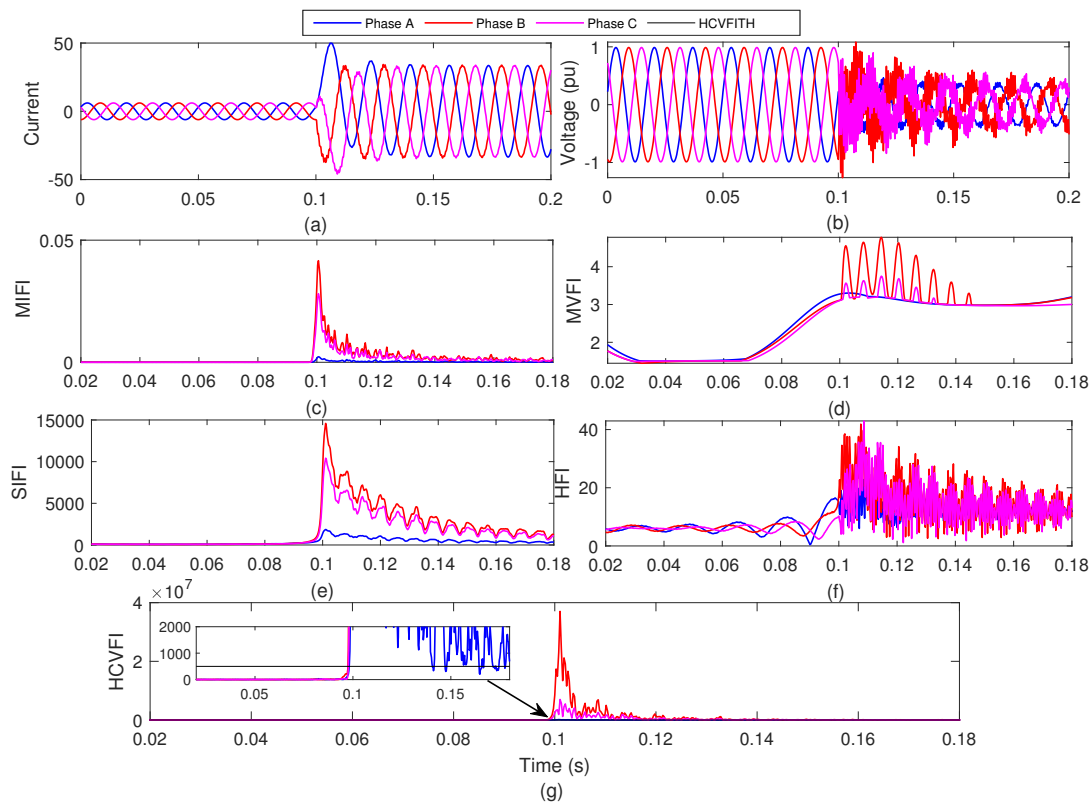


**Figure 6.** Estimation of ABC faults using the current- and voltage-actuated protection method. (a) Currents of all phases, (b) voltages of all phases, (c) MIFI, (d) MVFI, (e) SIFI, (f) HFI, and (g) HCVFI.

#### 4.1.5. ABCG Fault

An ABCG fault is realized at the center of the test line (75 km from bus-1). The currents and voltages of all phases are captured on bus-1 of the line. Current waveforms of all phases are depicted in Figure 7a. The voltage waveforms of all phases are depicted in Figure 7b. These currents and voltages are decomposed applying ST to compute MIFI, MVFI, and SIFI, which are detailed in Figure 7c–e, in respective sequence. The current and voltage signals are also decomposed using HT and Hilbert fault indices (HFI) are obtained, which is depicted in Figure 7f. The HCVFI is evaluated using the designed method which is depicted in Figure 7g.

Figure 7a indicates that currents of all phases are increased due to ABCG fault occurrence. Figure 7b details that the voltages associated with all phases are decreased due to ABCG fault occurrence. Figure 7c indicates that the MIFI of all phases are increased after ABCG fault occurrence. Figure 7d indicates that the MVFI of all phases are changed and deviate from a straight line nature. Figure 7e indicates that the SIFI of every phase is increased after ABCG fault occurrence. Figure 7f indicates that the HFI of all phases are increased after ABCG fault occurrence. Figure 7g indicates that the HCVFI of all phases are increased due to ABCG fault occurrence and become higher than the HCVFITH, indicating the faulty nature of all phases. Hence, ABCG faults are effectively identified using the proposed current- and voltage-actuated protection scheme.

The values of the HCVFI for all phases of an ABCG fault are included in Table 2. It is observed that the HCVFI for all phases have high values.

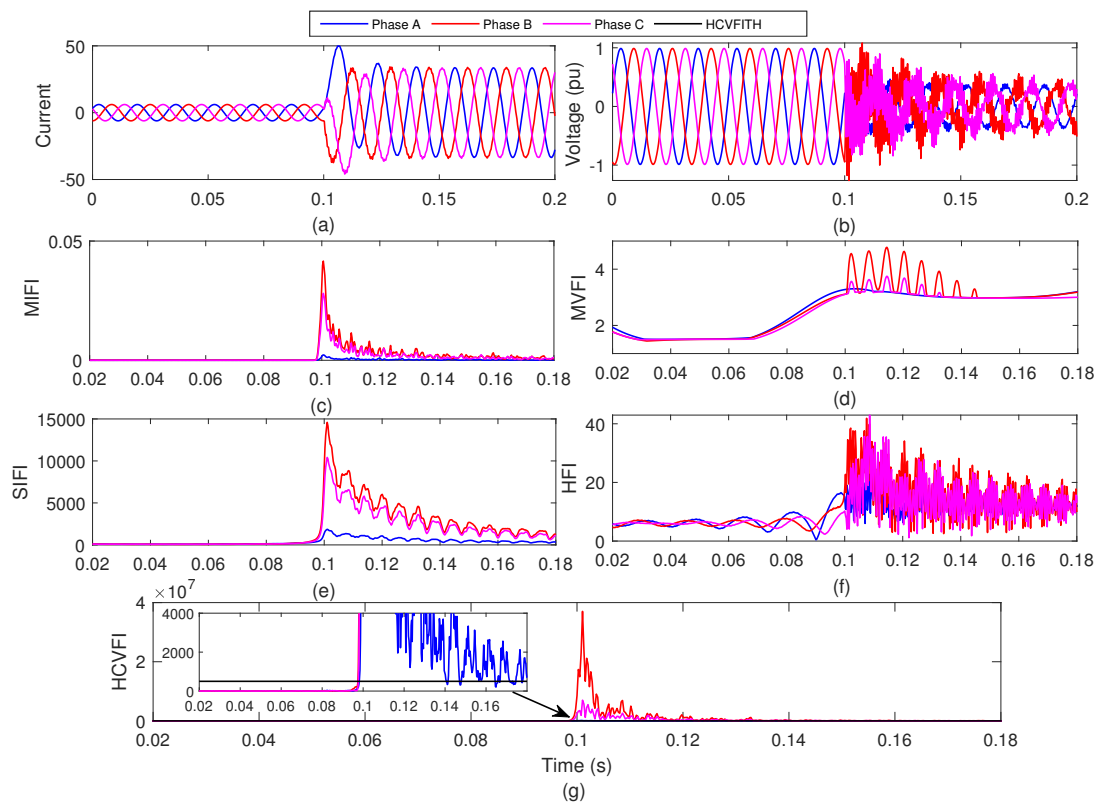


**Figure 7.** Estimation of ABCG faults using the current- and voltage-actuated protection method. (a) Currents of all phases, (b) voltages of all phases, (c) MIFI, (d) MVFI, (e) SIFI, (f) HFI, and (g) HCVFI.

#### 4.2. Fault Classification

Classification of faults is performed using the number of faulty phases and the index for ground detection (IGD). Faults involving one phase and ground are considered as single-phase-to-ground faults such as AG, BGs and CG. Faults involving two phases are considered as two-phase faults without involvement of ground (AB, BC, and CA) and with involvement of ground (ABG, BCG, and CAG). Faults involving all three phases are considered as three-phase faults without involvement of ground (ABC) and with involvement of ground (ABCG). Ground involvement during two-phase and three-phase faults is detected using IGD. IGD for the AB fault and ABG fault is described in Figure 8. It is seen that the IGD for an ABG fault is higher relative to the threshold for ground detection (THGD), which is equal to 1000, whereas the IGD is lower relative to THGD for an AB fault. Hence, all faults can be classified using the number of faulty phases and IGD.

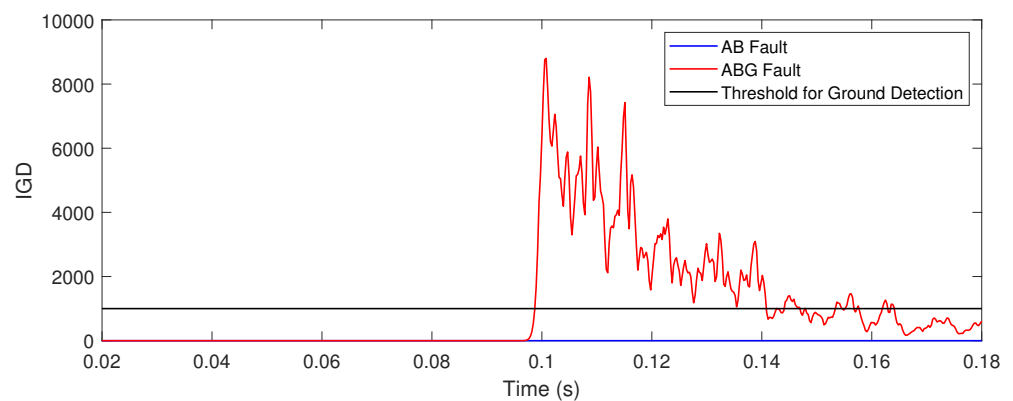


**Figure 8.** Index for ground detection.

## 5. Testing of the Algorithm in Various Case Studies

This section discusses the results of fault estimation for different case studies with different operating scenarios.

### 5.1. Impact of Variations in Fault Incidence Angle

To investigate an effect of variations in the fault occurrence angle, an AG fault is realized at the center of the line (75 km from bus-1) with a fault angle of  $45^\circ$ . Currents and voltages of all phases are recorded on bus-1 of the line. The currents of all phases are described in Figure 9a. The voltages of all phases are described in Figure 9b. The currents and voltages are decomposed by applying ST to compute MIFI, MVFI, and SIFI, which are detailed in Figure 9c–e, in respective order. The current and voltage waveforms are also decomposed using HT, and HFI are computed, which are detailed in Figure 9f. The proposed HCVFI is computed using the proposed method, which is illustrated in Figure 9g.

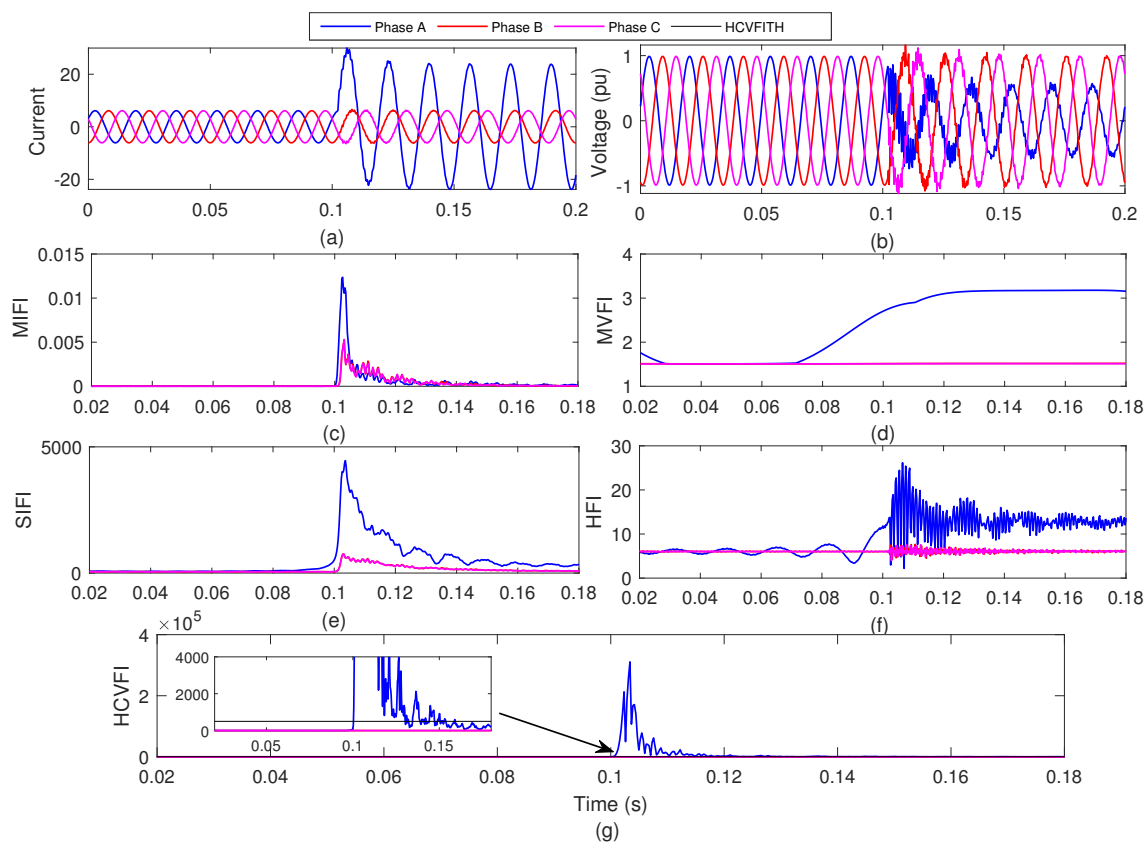


**Figure 9.** Estimation of AG faults with a fault angle of  $45^\circ$  using the current- and voltage-actuated protection method. (a) Currents of all phases, (b) voltages of all phases, (c) MIFI, (d) MVFI, (e) SIFI, (f) HFI, and (g) HCVFI.

Figure 9a indicates that the current of phase-A is increased due to AG faults with an angle of  $45^\circ$ , whereas the currents of phase-B and C retain their sinusoidal nature similar to the pre-fault period. Figure 9b indicates that voltage of phase-A is decreased due to occurrence of AG faults with an angle of  $45^\circ$ , whereas the voltages of phase-B and C retain their sinusoidal nature similar to the healthy period. Figure 9c indicates that the MIFI is increased due to occurrence of AG faults with an angle of  $45^\circ$ . Figure 9d indicates that the MVFI of phase-A is changed and deviates from a straight line nature. However, the MVFI of the healthy phase-B and C are similar to those in the pre-fault condition. Figure 9e indicates that the SIFI is increased due to the AG fault condition. However, the increase in the SIFI of the faulty phase-A is high compared to the healthy phase-B and C. Figure 9f indicates that the HFI of the faulty phase-A is increased due to the fault condition. However, the

HFI of the healthy phase-B and C are similar to the pre-fault condition. Figure 9g indicates that the HCVFI of the faulty phase-A is increased due to occurrence of AG faults with an angle of  $45^\circ$ , and becomes high relative to the HCVFITH, indicating the faulty nature of phase-A. However, the HCVFI of phase-B and C are lower relative to the HCVFITH, indicating the healthy nature of these phases. Hence, AG faults with an angle of  $45^\circ$  are effectively recognized using the proposed current- and voltage-actuated protection scheme.

To investigate the impact of variations in fault occurrence angles, an AG fault is realized at the center of the test power line (75 km from bus-1), considering a fault occurrence angle of  $90^\circ$ . Currents and voltages of all phases are captured on bus-1 of the power line. Currents of all phases are depicted in Figure 10a. Voltages of all phases are depicted in Figure 10b. These currents and voltages are decomposed by application of ST to compute MIFI, MVFI, and SIFI, which are detailed in Figure 10c–e, sequentially. Current and voltage signals are also processed using HT, and the HFI are computed, which is depicted in Figure 10f. The designed HCVFI is computed using the proposed method, which is illustrated in Figure 10g.

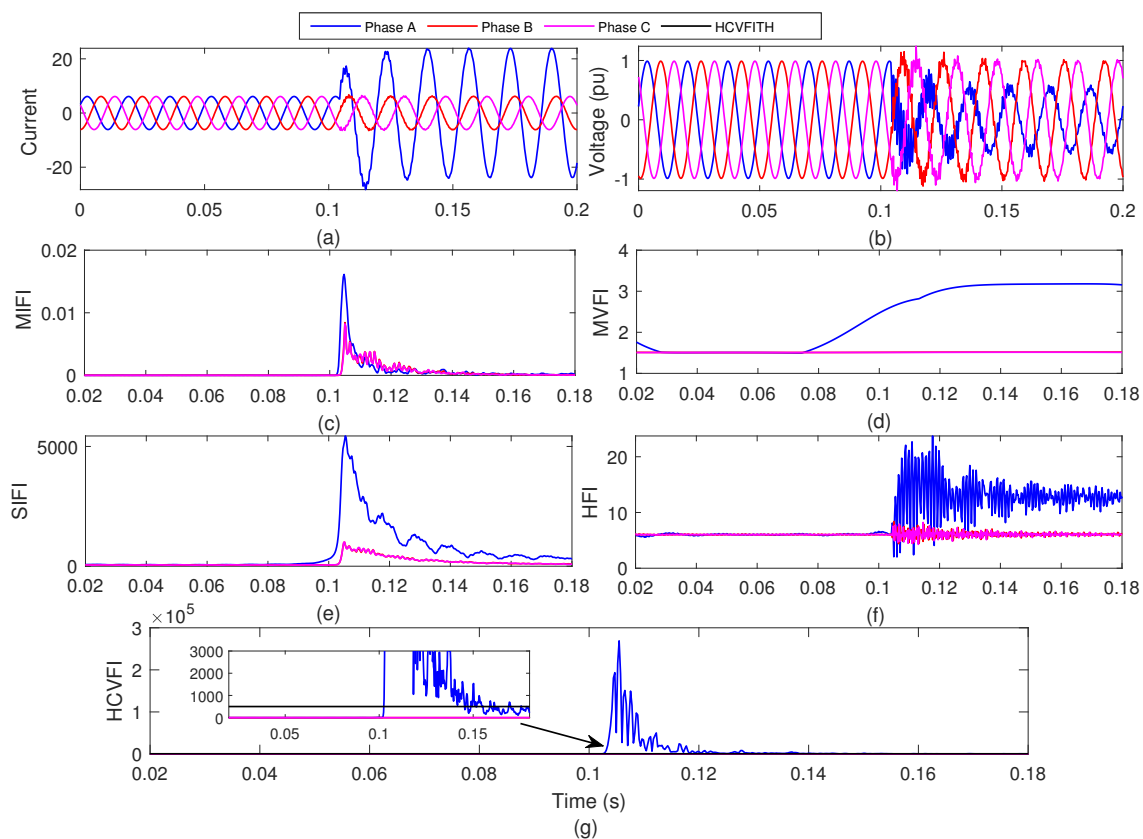


**Figure 10.** Estimation of AG faults with a fault incidence angle of  $90^\circ$  using the current- and voltage-actuated protection method. (a) Currents of all phases, (b) voltages of all phases, (c) MIFI, (d) MVFI, (e) SIFI, (f) HFI, and (g) HCVFI.

Figure 10a depicts that the current of phase-A is increased after occurrence of AG faults with a fault occurrence angle of  $90^\circ$ , whereas the magnitudes of the currents of phase-B and C follow a sinusoidal nature similar to that recorded in the healthy interval. Figure 10b depicts that the voltage of phase-A is decreased due to occurrence of AG faults with a fault occurrence angle of  $90^\circ$ , whereas the voltages of phase-B and C follow the sinusoidal nature similar to the healthy interval. Figure 10c details that the MIFI is increased due to occurrence of AG faults with a fault occurrence angle of  $90^\circ$ . Figure 10d indicates that the MVFI of the faulty phase-A is changed and deviates from a straight line nature. However, the MVFI of the healthy phase-B and C are similar to those seen in the pre-fault condition.

Figure 10e indicates that the SIFI is increased due to occurrence of AG faults. However, the increase in the SIFI of the faulty phase-A is high relative to the healthy phase-B and C. Figure 10f indicates that the HFI of the faulty phase-A is increased due to occurrence of the fault. However, the HFI of the healthy phase-B and C are similar to those of pre-fault scenario. Figure 10g indicates that the HCVFI of the faulty phase-A is increased due to occurrence of the fault condition considering a fault occurrence angle of  $90^\circ$ , and becomes high relative to the threshold HCVFITH, which indicates the faulty nature of phase-A. However, the HCVFI of phase-B and C are similar to the pre-fault scenario and lower than the HCVFITH, which indicates the healthy nature of the phases. Hence, AG fault incidents with a fault occurrence angle of  $90^\circ$  are effectively recognized using the proposed current- and voltage-actuated protection scheme.

the designed current- and voltage-actuated fault recognition algorithm is tested to detect AG fault incidents in the middle of the test transmission line with fault incidence angles of  $0^\circ$ ,  $30^\circ$ ,  $60^\circ$ ,  $90^\circ$ ,  $120^\circ$ ,  $150^\circ$ , and  $180^\circ$ . Peak magnitudes of HCVFI for all phases during these different conditions are included in Table 3. It is observed that the peak magnitude of the HCVFI for phase-A with investigated fault incidence angle is higher than the HCVFITH, whereas the peak magnitude of the HCVFI for phase-B and C is lower than the HCVFITH. Hence, the proposed fault detection method is effective in detecting faults for all possible fault incidence angles on a half cycle. The next half cycle is a mirror image of the of the first half cycle. Hence, the algorithm is also effective in detecting faults on the next half cycle, and, ultimately over the entire cycle.

**Table 3.** Magnitudes of HCVFI for AG faults with different fault incidence angles.

Fault Incidence Angle	HCVFI		
	Phase-A	Phase-B	Phase-C
$0^\circ$	$1.1596 \times 10^5$	$2.9253 \times 10^{-9}$	$6.1953 \times 10^{-10}$
$30^\circ$	$1.5729 \times 10^5$	$1.6947 \times 10^{-7}$	$1.9282 \times 10^{-8}$
$60^\circ$	$2.6444 \times 10^5$	$2.1137 \times 10^{-6}$	$2.5749 \times 10^{-7}$
$90^\circ$	$2.9118 \times 10^5$	$1.7011 \times 10^{-6}$	$1.2399 \times 10^{-7}$
$120^\circ$	$2.7605 \times 10^5$	$2.4511 \times 10^{-7}$	$5.4373 \times 10^{-8}$
$150^\circ$	$1.8069 \times 10^5$	$2.3092 \times 10^{-8}$	$4.0983 \times 10^{-8}$
$180^\circ$	$1.4967 \times 10^5$	$3.2953 \times 10^{-9}$	$5.0839 \times 10^{-10}$

### 5.2. Fault Impedance Variations

To investigate the effect of variations in fault impedance, an AG fault is realized at the center of the test power line (75 km from node-1), considering a fault impedance of  $5 \Omega$ . The currents of all phases are depicted in Figure 11a. The voltages of all phases are depicted in Figure 11b. These currents and voltages are decomposed using ST to compute MIFI, MVFI, and SIFI, which are depicted in Figure 11c–e, sequentially. The current and voltage waveforms are also decomposed using HT and the HFI are computed, which is depicted in Figure 11f. The proposed HCVFI is computed using the designed method, which is depicted in Figure 11g.

Figure 11a depicts that the current of phase-A is increased after occurrence of AG faults with a fault impedance of  $5 \Omega$ , whereas the currents of phase-B and C follow the sinusoidal nature similar to the healthy period. Figure 11b indicates that the voltage of phase-A is decreased after occurrence of AG faults with a fault impedance of  $5 \Omega$ , whereas the voltages of phase-B and C follow a sinusoidal nature similar to the healthy period. Figure 11c indicates that the MIFI is increased after occurrence of AG faults considering a fault impedance of  $5 \Omega$ . Figure 11d indicates that the MVFI of the faulty phase-A is changed and deviates from a straight line nature. However, the MVFI of the healthy phase-B and C are the same as those of the pre-fault condition. Figure 11e indicates that the SIFI is

increased after occurrence of AG fault condition with a fault impedance of  $5 \Omega$ . However, increase in the SIFI for the faulty phase-A is high compared to the healthy phase-B and C. Figure 11f indicates that the HFI of the faulty phase-A is increased after occurrence of fault. However, the HFI of the healthy phase-B and C is similar in the post-fault condition and in the pre-fault scenario. Figure 11g indicates that the HCVFI of the faulty phase-A is increased after occurrence of fault considering a fault impedance of  $5 \Omega$  and becomes high relative to the threshold HCVFITH, indicating the faulty nature of phase-A. However, the HCVFI of the healthy phase-B and C are similar to those in the pre-fault condition and low relative to the HCVFITH, indicating healthiness of these phases. Hence, AG fault occurrence with a fault impedance of  $5 \Omega$  is effectively recognized using the designed current- and voltage-actuated protection scheme.

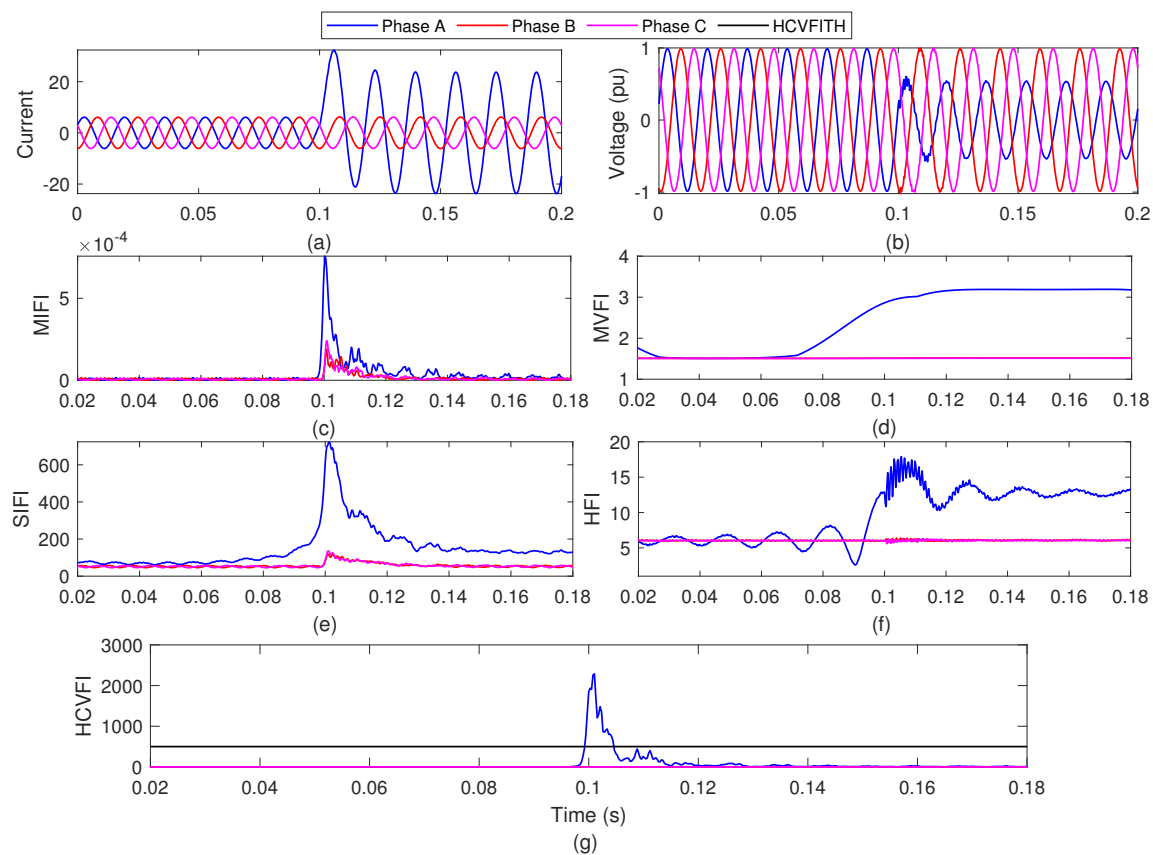


**Figure 11.** Estimation of AG faults with a fault impedance of  $5 \Omega$  using the current- and voltage-actuated protection method. (a) Currents of all phases, (b) voltages of all phases, (c) MIFI, (d) MVFI, (e) SIFI, (f) HFI, and (g) HCVFI.

The designed current- and voltage-actuated fault recognition algorithm is tested to detect AG fault incidents in the middle of the test transmission line with fault impedances of  $0 \Omega$ ,  $2 \Omega$ ,  $4 \Omega$ ,  $6 \Omega$ ,  $8 \Omega$ ,  $10 \Omega$ , and  $50 \Omega$ . Peak magnitudes of the HCVFI for all phases with different fault impedances are included in Table 4. It is observed that the peak magnitudes of the HCVFI for phase-A with the investigated fault impedances are higher than the HCVFITH, whereas the peak magnitudes of the HCVFI for phase-B and C are lower than HCVFITH. Hence, the proposed fault detection method is effective in detecting faults for fault impedances as high as  $50 \Omega$ .

**Table 4.** Magnitudes of HCVFI for AG faults with different fault impedances.

Fault Impedance	HCVFI		
	Phase-A	Phase-B	Phase-C
0 $\Omega$	$1.1596 \times 10^5$	$2.9253 \times 10^{-9}$	$6.1953 \times 10^{-10}$
2 $\Omega$	$7.0187 \times 10^4$	$2.9450 \times 10^{-9}$	$5.1641 \times 10^{-10}$
4 $\Omega$	$4.0913 \times 10^4$	$2.8969 \times 10^{-9}$	$4.2383 \times 10^{-10}$
6 $\Omega$	$2.9786 \times 10^4$	$2.8140 \times 10^{-9}$	$3.4607 \times 10^{-10}$
8 $\Omega$	$4.0558 \times 10^4$	$2.7107 \times 10^{-9}$	$2.8331 \times 10^{-10}$
10 $\Omega$	$5.4548 \times 10^4$	$2.5949 \times 10^{-9}$	$2.3555 \times 10^{-10}$
50 $\Omega$	$6.3866 \times 10^3$	$7.3598 \times 10^{-10}$	$1.9503 \times 10^{-10}$

### 5.3. Fault Location Variations

To investigate the impact of variations in fault location, an AG fault is realized at a location of 30 km from bus-1. The currents of all phases are illustrated in Figure 12a. The voltages associated with all phases are detailed in Figure 12b. These currents and voltages are decomposed with the help of ST to compute MIFI, MVFI, and SIFI, which are detailed in Figure 12c–e, sequentially. The current and voltage signals are also decomposed using HT and HFI are computed, which is detailed in Figure 12f. The proposed HCVFI is computed using the proposed method, which is detailed in Figure 12g.

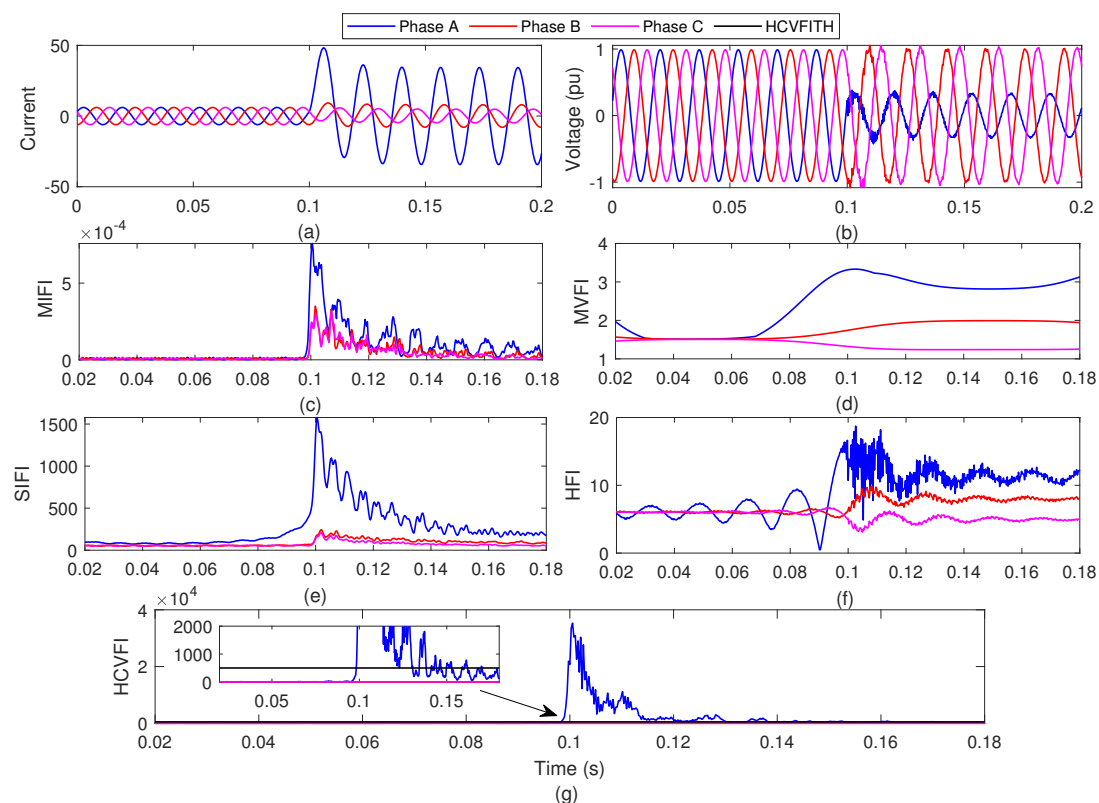


**Figure 12.** Estimation of AG fault incidents at a location of 30 km from the sending terminal of the transmission line using the current- and voltage-actuated protection method. (a) Currents of all phases, (b) voltages of all phases, (c) MIFI, (d) MVFI, (e) SIFI, (f) HFI, and (g) HCVFI.

Figure 12a indicates that the current of phase-A is increased after occurrence of AG faults at a location of 30 km from bus-1, whereas the currents of phase-B and C follow the sinusoidal nature similar to the healthy period. Figure 12b indicates that the voltage

of phase-A is decreased after occurrence of AG faults at a location of 30 km from bus-1, whereas the voltages of phase-B and C follow a sinusoidal nature similar to the healthy period. Figure 12c details that the MIFI is increased after occurrence of AG faults at a location of 30 km from bus-1. Figure 12d indicates that the MVFI of the faulty phase-A is changed and deviates from a straight line nature. However, the MVFI of the healthy phase-B and C is similar to the pre-fault condition. Figure 12e indicates that the SIFI is increased after occurrence of AG fault condition at a location of 30 km from bus-1. However, the increase in the SIFI of the faulty phase-A is high relative to the healthy phase-B and C. Figure 12f details that the HFI of the faulty phase-A is increased after occurrence of fault. However, the HFI of the healthy phase-B and C is similar to the pre-fault condition. Figure 12g indicates that HCVFI of the faulty phase-A is increased after occurrence of fault at a location of 30 km from bus-1 and becomes high relative to the HCVFITH, indicating the faulty nature of phase-A. However, the HCVFI for the healthy phase-B and C is similar to the pre-fault scenario and low relative to the HCVFITH, indicating the healthy nature of the phases. Hence, AG faults occurring at a location of 30 km from bus-1 are effectively recognized using the designed current- and voltage-actuated protection scheme.

to investigate the effect of variations in fault location, an AG fault is realized at location of 120 km from bus-1. The currents of all phases are depicted in Figure 13a. The voltages of all phases are depicted in Figure 13b. These currents and voltages are decomposed with the help of ST to compute MIFI, MVFI, and SIFI, which are detailed in Figure 13c–e, in respective order. The current and voltage signals are also decomposed using HT and HFI are computed, which is depicted in Figure 13f. The proposed HCVFI is computed using the proposed method, which is illustrated in Figure 13g.

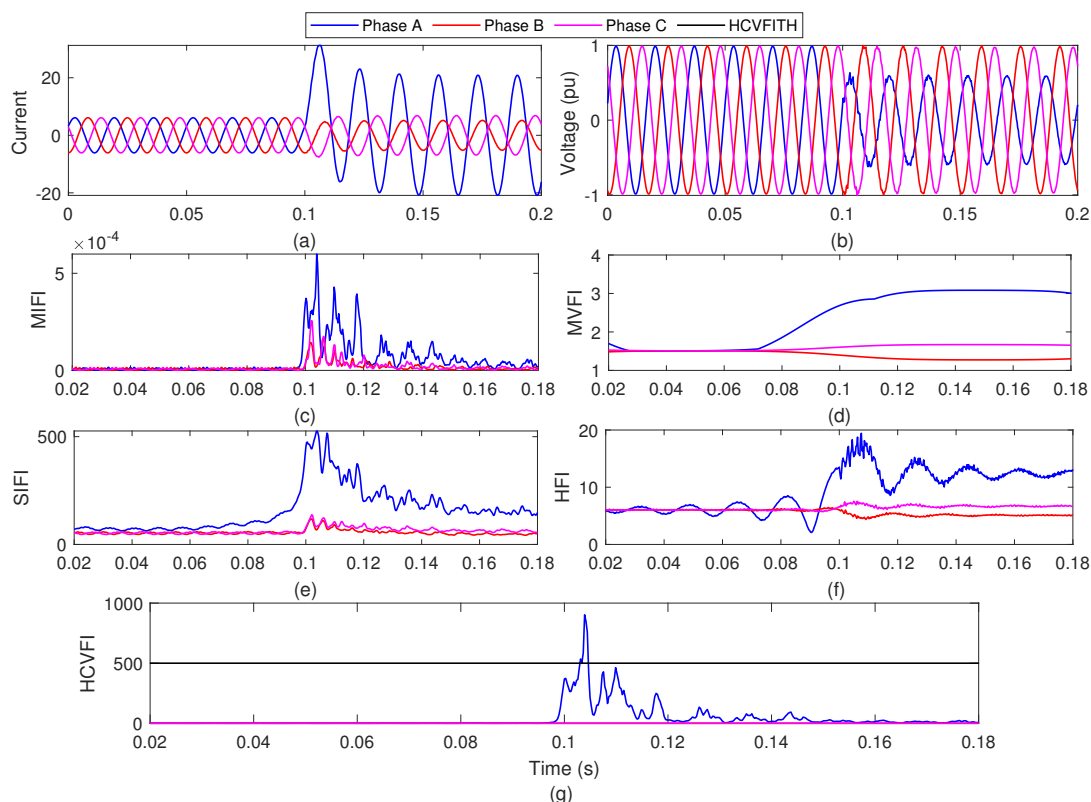


**Figure 13.** Estimation of AG fault incidents at a location of 120 km from the sending terminal of the power line using the current- and voltage-actuated protection method. (a) Currents of all phases, (b) voltages of all phases, (c) MIFI, (d) MVFI, (e) SIFI, (f) HFI, and (g) HCVFI.

Figure 13a indicates that the current of phase-A is increased after occurrence of AG faults at a location of 120 km from bus-1, whereas the currents of phase-B and C follow

the sinusoidal nature similar to the healthy period. Figure 13b indicates that the voltage of phase-A is decreased after occurrence of AG faults at a location of 120 km from bus-1, whereas the voltages of phase-B and C follow the sinusoidal nature similar to the healthy period. Figure 13c indicates that the MIFI is increased after occurrence of AG faults at a location of 120 km from bus-1. Figure 13d indicates that the MVFI of the faulty phase-A is changed and deviates from a straight line nature. However, the MVFI of the healthy phase-B and C are similar to the pre-fault condition. Figure 13e indicates that the SIFI is increased after occurrence of AG faults at a location of 120 km from bus-1. However, increase in the SIFI of the faulty phase-A is high relative to phase-B and C. Figure 13f depicts that the HFI of the faulty phase-A is increased after occurrence of the fault. However, the HFI of the healthy phase-B and C are similar to the pre-fault condition. Figure 13g indicates that the HCVFI of the faulty phase-A is increased after occurrence of fault at a location of 120 km from bus-1 and becomes high relative to HCVFITH, indicating the faulty nature of phase-A. However, the HCVFI for the healthy phase-B and C is the same as in the pre-fault condition and low relative to the HCVFITH, indicating the healthy nature of the phases. Hence, AG faults occurring at a location of 120 km from bus-1 are effectively recognized using the proposed current- and voltage-actuated protection scheme.

The designed current- and voltage-actuated fault recognition algorithm is tested to detect AG fault incidents at locations 20 km, 40 km, 60 km, 80 km, 100 km, 120 km, and 140 km away from the sending end bus-1 of the test transmission. Peak magnitudes of the HCVFI for all phases with different fault locations are included in Table 5. It is observed that the peak magnitudes of the HCVFI for phase-A with the investigated fault locations is higher than the HCVFITH, whereas the peak magnitudes of the HCVFI for phase-B and C are lower than the HCVFITH. Hence, the proposed fault detection method is effective in detecting fault incidents on every location of the transmission line.

**Table 5.** Magnitudes of HCVFI for AG faults at different fault locations.

Fault Location	HCVFI		
	Phase-A	Phase-B	Phase-C
20 km	$8.1529 \times 10^6$	0.0098	0.0191
40 km	$8.0364 \times 10^5$	$3.6033 \times 10^{-4}$	0.0011
60 km	$1.7889 \times 10^5$	$3.6384 \times 10^{-6}$	$1.7873 \times 10^{-5}$
80 km	$1.1774 \times 10^5$	$9.2254 \times 10^{-8}$	$6.3385 \times 10^{-8}$
100 km	$7.3322 \times 10^4$	$9.2265 \times 10^{-6}$	$7.0646 \times 10^{-5}$
120 km	$5.1786 \times 10^4$	$3.0758 \times 10^{-4}$	0.0056
140 km	$4.6031 \times 10^4$	0.0048	0.2228

## 6. Testing of the Algorithm on a Practical Transmission Line

The fault detection approach of the designed protection scheme is tested on a 180 km long practical line operated on a 400kV voltage level and connected between a 400 kV Grid sub-station (GSS), Jodhpur, and a 400 kV GSS, Kankroli, of the utility transmission network in Rajasthan, India. Interconnection of the transmission lines and generation lines at 400 kV GSS, Kankroli, and 400 kV GSS, Jodhpur, is illustrated in Figure 14. The 400 kV test transmission line between Kankroli and Jodhpur is a single circuit (S/C) line with a surge impedance loading (SIL) rating equal to 515 MW. This test line is part of a large-area practical utility network. Details of the grid sub-station, circuit length of transmission lines, and installed capacity of generation sources of Rajasthan transmission system are included in Tables 6–8, [16] respectively. Details of generation, transmission network, transformers, and loads of the practical utility network used for the study are available in [12].

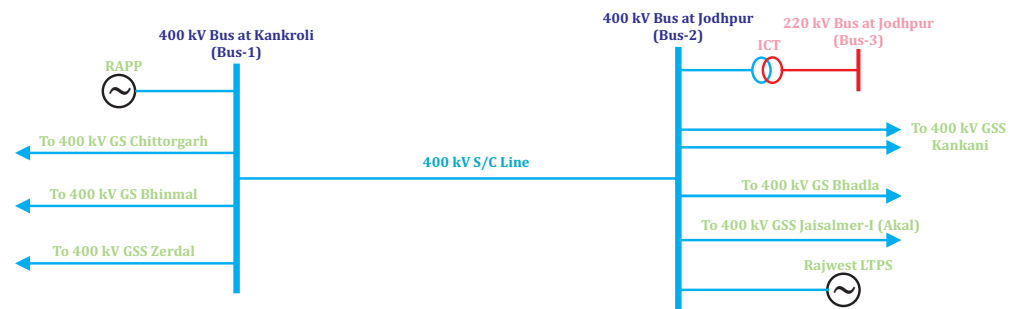


**Figure 14.** The 400kV S/C Jodhpur–Kankroli practical transmission line of the Indian Grid.

**Table 6.** Number of extra-high voltage grid sub-stations.

Sr. No.	Voltage Level of GSS	Total Number of Existing GSS	Total Number of under Construction GSS
1	765 kV	2	2
2	400 kV	18	6
3	220 kV	128	22
4	132 kV	469	44
Total	-	617	74

**Table 7.** Circuit length of extra-high voltage transmission lines.

Sr. No.	Voltage Level of GSS	Length of Existing Lines (Circuit km)	Length of under Construction Lines (Circuit km)
1	765 kV	2	2
2	400 kV	18	6
3	220 kV	128	22
4	132 kV	469	44
Total	-	617	74

**Table 8.** Source-wise installed capacity of generation [16].

Sr. No.	Capacity (MW)	Percentage Contribution
Coal-based power plant	13284.368	57%
Gas-based power plant	603.50	3%
Nuclear power plant	456.74	2%
Hydro power plant	1961.954	8%
Wind power plant	3730.35	16%
Biomass power plant	101.95	0.43%
Solar power plant	3288.10	14%
Small-size solar power plant	60.50	0.26%

The algorithm is tested on the practical 400 kV S/C Jodhpur–Kankroli practical transmission line of the Indian Grid illustrated in Figure 15. The current and voltage waveforms for a period of 12 cycles, which includes 6 pre-fault time cycles and 6 post-fault time cycles, are captured from the fault recorders installed on the transmission line at the 400 kV GSS Jodhpur end of the line. The current waveform is decomposed using the designed algorithm to compute the HCVFI which is depicted in Figure 15. It is observed that the

maximum magnitude of the HCVFI is greater than the HCVFITH for phase-A. The peak value of the HCVFI is lower than the HCVFITH for phase-B and C. Hence, the proposed method effectively identifies fault event incidents on a practical power line of a large-area real-time utility network.

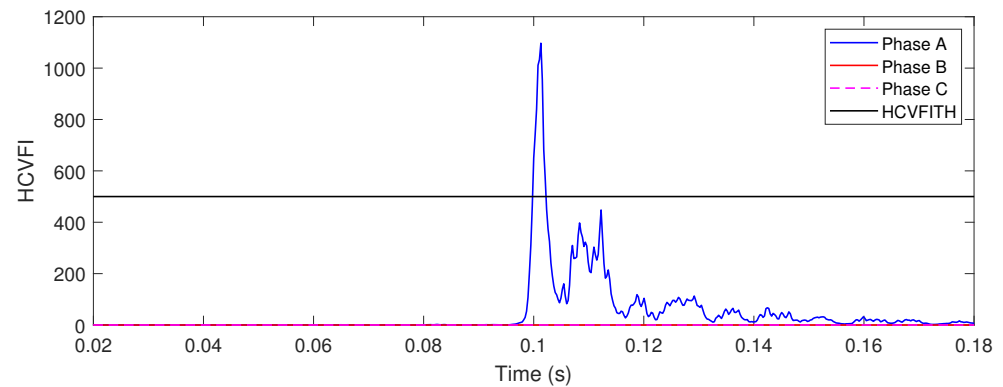


**Figure 15.** HCVFI for an AG fault incident on a practical transmission line.

## 7. Performance Comparison

The performance of the proposed method used for fault detection is compared to a discrete wavelet transform (DWT)-based approach. It is established that the DWT-based protection scheme reported in [17] is effective with a noise level of 40 dB SNR (signal to noise ratio) and lower. Our proposed method is effective for detecting faults efficiently even in the presence of high noise levels of 20dB SNR. Hence, the performance of the designed method is better relative to DWT-based methods. The performance of the proposed method is also compared with a time–frequency-based transmission line protection method [18] and an alienation-based transmission line protection method [19]. A comparative study on the performance, considering parameters such as impact of noise on the performance of the algorithm, sampling frequency, classification of faults, impact of fault impedance, impact of fault incidence angle, impact of fault location, and validation of algorithm on a real-time network is included in Table 9 [16]. It is observed that the proposed method performs better compared to the methods reported in [17–19] in terms of the investigated indicators.

**Table 9.** Comparative study on the performance of different protection algorithms [16].

Sr. No.	Indicative Parameter	Reference			Proposed Method
		[17]	[18]	[19]	
1	Noise level for which performance of algorithm is not affected (SNR)	40 dB SNR	SNR not defined	Not investigated	20 dB SNR
2	Sampling frequency (kHz)	3.84 kHz	3.84 kHz	Not mentioned	3.84 kHz
3	Classification of faults	Investigated	Investigated	Investigated	Investigated
4	Impact of fault incidence angle	Investigated	Not investigated	Investigated	Investigated
5	Impact of fault impedance	Investigated	Investigated	Not investigated	Investigated
6	Impact of fault location	Investigated	Investigated	Investigated	Investigated
7	Validation of algorithm on real-time network	Not performed	Not performed	Not performed	Performed

## 8. Conclusions

This paper introduced an algorithm using current and voltage signals for identification of faults on a power transmission line. Current and voltage waveforms associated with all phases are decomposed with the help of ST and the proposed MIFI, MVIFI, and SIFI

are computed. The current and voltage waveforms are also processed using HT and HFI are computed. The proposed hybrid current and voltage fault index (HCVFI) is computed using MIFI, MVFI, SIFI, and HFI. A threshold magnitude for hybrid current and voltage fault index (HCVFIT) of 500 is chosen for the HCVFI to differentiate fault events from healthy scenarios. This HCVFIT is selected by testing the algorithm for various scenarios such as fault location, impedance of fault, fault occurrence angle, and reverse power flow. It is concluded that the designed protection method is effective for identification of faults including AG, AB, ABG, ABC, and ABCG. The algorithm is also effective for detection of faults for scenarios such as fault occurrence angle variations, different fault impedances, and different fault locations. The proposed method is effective in classifying and discriminating faults by considering the number of faulty phases and the IGD. The algorithm effectively detected an AG fault event that occurred on a practical power line. The performance of the designed method is better compared to a DWT-based algorithm, a time-frequency approach, and an alienation method. Further, hybridization of different features of voltage and current extracted using additional methods such as alienation coefficients in conjunction with ST and HT might improve the performance of the algorithm, which may be considered as future research scope of the study. Use of artificial intelligence, machine learning, and deep learning approaches may also improve the fault classification accuracy which may also be investigated in future work.

**Author Contributions:** Conceptualization, L.T. and O.P.M.; methodology, L.T.; software, L.T.; validation, L.T., B.K. and O.P.M.; formal analysis, L.T.; investigation, L.T.; resources, B.K.; data curation, L.T.; writing—original draft preparation, L.T.; writing—review and editing, L.T. and O.P.M.; visualization, B.K.; supervision, Y.M.; project administration, L.T.; funding acquisition, L.T. All authors have read and agreed to the published version of the manuscript.

**Funding:** This work was sponsored in part by the National Natural Science Foundation of China (61871178) and the Enterprise Action Plan for young teachers in colleges and universities of Hubei Province (XD2014673).

**Institutional Review Board Statement:** Not applicable.

**Informed Consent Statement:** Not applicable.

**Data Availability Statement:** Data is contained within the article.

**Conflicts of Interest:** The authors declare no conflict of interest.

## Abbreviations

The following abbreviations are used in this manuscript:

AB	Phase-A to phase-B fault
ABC	Three-phase fault without involving ground
ABCG	Three-phase fault involving ground
ABG	Phase-A and phase-B to ground fault
AC	Alternating current
AG	Phase-A to ground fault
CB	Circuit breakers
CCI	Current-based co-variance index
CMI	Current-based median index
CMVI	Current-based maximum value index
CSI	Current-based summation index
CT	Current transformer
CVIFI	Co-variance intermediate fault index
CVZSI	Co-variance zero sequence index
CWT	Continuous wavelet transform

DL	Deep learning
DRNN	Deep recurrent neural networks
DWT	Discrete wavelet transform
FACTS	Flexible AC transmission system
FFG	First fault group
FLP	Fault location prediction
FRI	Fault region identification
FTC	Fault type classification
GSS	Grid sub-station
HCI	Hilbert current index
HCVFI	Hybrid current and voltage fault index
HCVFITH	Threshold value for the hybrid current and voltage fault index
HFI	Hilbert fault index
HIF	High impedance faults
HIFI	Hilbert intermediate fault index
HT	Hilbert transform
IGD	Index for ground detection
ISTS	Inter-state transmission line
LDA	Linear discriminant analysis
MIFI	Median intermediate fault index
MVFI	Maximum value intermediate fault index
MVZSI	Maximum value zero sequence index
MZSI	Median zero sequence index
PT	Potential transformer
RE	Renewable energy
SAT-CNN	Self-attention convolutional neural network
SFG	Second fault ground
SIFI	Summation intermediate fault index
SNR	Signal to noise ratio
ST	Stockwell transform
STATCOM	Static synchronous compensator
STFT	Short time Fourier transform
SZSI	Summation zero sequence index
THGD	Threshold for ground detection
TFG	Third fault group
UG	Utility generator
VCI	Voltage-based co-variance index
VMI	Voltage-based median index
VMVI	Voltage-based maximum value index
VSI	Voltage-based summation index
WF	Weight factor
WT	Wavelet transform

## References

1. Fahim, S.R.; Sarker, S.K.; Muyeen, S.; Das, S.K.; Kamwa, I. A deep learning based intelligent approach in detection and classification of transmission line faults. *Int. J. Electr. Power Energy Syst.* **2021**, *133*, 107102. [[CrossRef](#)]
2. Kumar, B.R.; Mohapatra, A.; Chakrabarti, S.; Kumar, A. Phase angle-based fault detection and classification for protection of transmission lines. *Int. J. Electr. Power Energy Syst.* **2021**, *133*, 107258. [[CrossRef](#)]
3. Fahim, S.R.; Sarker, Y.; Sarker, S.K.; Sheikh, M.R.I.; Das, S.K. Self attention convolutional neural network with time series imaging based feature extraction for transmission line fault detection and classification. *Electr. Power Syst. Res.* **2020**, *187*, 106437. [[CrossRef](#)]
4. Mousaviyan, I.; Seifossadat, S.G.; Saniei, M. Traveling Wave-based Algorithm for Fault Detection, Classification, and Location in STATCOM-Compensated Parallel Transmission Lines. *Electr. Power Syst. Res.* **2022**, *210*, 108118. [[CrossRef](#)]
5. El-Zonkoly, A.; Desouki, H. Wavelet entropy based algorithm for fault detection and classification in FACTS compensated transmission line. *Int. J. Electr. Power Energy Syst.* **2011**, *33*, 1368–1374. [[CrossRef](#)]
6. Belagoune, S.; Bali, N.; Bakdi, A.; Baadji, B.; Atif, K. Deep learning through LSTM classification and regression for transmission line fault detection, diagnosis and location in large-scale multi-machine power systems. *Measurement* **2021**, *177*, 109330. [[CrossRef](#)]

7. Zhao, H.; Jiang, Y.; Zhang, F.; Zheng, W.; Fang, B.; He, M.; Wang, N. Quality Optimization of Transmission Line Fault Detection Algorithm based on Embedded Chip. In Proceedings of the 2021 International Conference on Control Science and Electric Power Systems (CSEPS), Shanghai, China, 28–30 May 2021; pp. 79–82. [\[CrossRef\]](#)
8. Jangir, S.; Choudhary, R.; Rathore, B.; Shaik, A.G. Transmission Line Fault Detection and Classification Using Alienation Coefficient Technique for Current Signals. In Proceedings of the 2018 3rd International Conference for Convergence in Technology (I2CT), Pune, India, 6–8 April 2018; pp. 1–6. [\[CrossRef\]](#)
9. Althi, T.R.; Koley, E.; Ghosh, S. Fuzzy Logic based Fault Detection and Classification scheme for Series Faults in Six Phase Transmission Line. In Proceedings of the 2021 7th International Conference on Electrical Energy Systems (ICEES), Chennai, India, 11–13 February 2021; pp. 479–483. [\[CrossRef\]](#)
10. Yadav, A.; Swetapadma, A. A novel transmission line relaying scheme for fault detection and classification using wavelet transform and linear discriminant analysis. *Ain Shams Eng. J.* **2015**, *6*, 199–209. [\[CrossRef\]](#)
11. Kumar, A.; Sharma, H.; Mahia, R.N.; Mahela, O.P.; Khan, B. Design and implementation of hybrid transmission line protection scheme using signal processing techniques. *Int. Trans. Electr. Energy Syst.* **2022**, *2022*, 7209553. [\[CrossRef\]](#)
12. Ola, S.R. Wigner distribution function and alienation coefficient-based transmission line protection scheme. *IET Gener. Transm. Distrib.* **2020**, *14*, 1842–1853. [\[CrossRef\]](#)
13. Mahela, O.P.; Shaik, A.G. Recognition of power quality disturbances using S-transform based ruled decision tree and fuzzy C-means clustering classifiers. *Appl. Soft Comput.* **2017**, *59*, 243–257. [\[CrossRef\]](#)
14. Stockwell, R.G.; Mansinha, L.; Lowe, R.P. Localization of the complex spectrum: The S transform. *Signal Process. IEEE Trans.* **1996**, *44*, 998–1001. [\[CrossRef\]](#)
15. Lee, I.W.C.; Dash, P.K. S-transform-based intelligent system for classification of power quality disturbance signals. *Ind. Electron. IEEE Trans.* **2003**, *50*, 800–805. [\[CrossRef\]](#)
16. Gupta, A.; Pachar, R.K.; Khan, B.; Mahela, O.P.; Padmanaban, S.; IET, F. A multivariable transmission line protection scheme using signal processing techniques. *IET Gener. Transm. Distrib.* **2021**, *15*, 3115–3137. [\[CrossRef\]](#)
17. Shaik, A.G.; Pulipaka, R.R.V. A new wavelet based fault detection, classification and location in transmission lines. *Int. J. Electr. Power Energy Syst.* **2015**, *64*, 35–40. [\[CrossRef\]](#)
18. Dash, P.; Moirangthem, J.; Das, S. A new time–frequency approach for distance protection in parallel transmission lines operating with STATCOM. *Int. J. Electr. Power Energy Syst.* **2014**, *61*, 606–619. [\[CrossRef\]](#)
19. Rathore, B.; Shaik, A.G. Alienation based fault detection and classification in transmission lines. In Proceedings of the 2015 Annual IEEE India Conference (INDICON), New Delhi, India, 17–20 December 2015; pp. 1–6. [\[CrossRef\]](#)

**Disclaimer/Publisher’s Note:** The statements, opinions and data contained in all publications are solely those of the individual author(s) and contributor(s) and not of MDPI and/or the editor(s). MDPI and/or the editor(s) disclaim responsibility for any injury to people or property resulting from any ideas, methods, instructions or products referred to in the content.